

RESEARCH ARTICLE



View Article Online

View Journal | View Issue



Cite this: *Inorg. Chem. Front.*, 2017, 4, 2059

Synthesis of a ceria-supported iron–ruthenium oxide catalyst and its structural transformation from subnanometer clusters to single atoms during the Fischer–Tropsch synthesis reaction†

Xu Wang,^{a,b} Xin-Pu Fu,^c Wen-Zhu Yu,^c Chao Ma,^{*d} Chun-Jiang Jia ^{*c} and Rui Si ^{*a}

The formation of supported metal/metal oxide single-atom catalysts (SAC), as well as their structural evolution during catalytic reactions have attracted much research interest in the fields of both inorganic chemistry and catalysis recently. In this work, we report the synthesis of iron (ca. 10 at%) oxide catalysts with the doping of a small amount (0.5–0.6 at%) of ruthenium oxide, which have been deposited onto the surface of ceria nanorods by an optimized deposition–precipitation (DP) route. Multiple characterization studies including X-ray diffraction (XRD), high-resolution transmission electron microscopy (HRTEM) and nitrogen adsorption/desorption confirmed the identical structural and textural properties of the ceria support after the DP step. Aberration-corrected high-angle annular dark-field scanning transmission electron microscopy (HAADF-STEM) combined with electron energy loss spectroscopy (EELS) showed the formation of subnanometer iron species in the fresh samples. Furthermore, the X-ray absorption fine structure (XAFS) technique with the help of related data analysis verified the generation of noncrystalline iron oxide clusters predominantly composed of Fe³⁺ ions. Here, the addition of a secondary metal (ruthenium) greatly promoted the dispersion of Fe over the ceria nanorods. After the catalytic reaction of Fischer–Tropsch synthesis (FTS), the transformation from subnanometer iron oxide species to ionic Fe⁶⁺ single atoms has been revealed and confirmed by the corresponding profile fits on the extended X-ray absorption fine structure (EXAFS) spectra. In contrast to the normal coarsening process, the FTS conditions (up to 300 °C, 2 MPa, CO/H₂ = 1/1) did drive the creation of such iron single atoms solely coordinated by oxygen ions.

Received 8th August 2017,
Accepted 10th October 2017

DOI: 10.1039/c7qi00470b

rscl.li/frontiers-inorganic

Introduction

Recently, supported metal/metal oxide single-atom catalysts (SAC) have attracted much research interest because of their unique electronic and/or local coordination structure, as well as their potential applications in multiple catalytic processes, which is probably due to 100% exposed active sites and/or new reaction pathways.^{1–23} So, both the development of the fabrica-

tion of SAC and deepening of the understanding of the formation mechanism on such single-atom species are of significant importance in heterogeneous catalysis. Various wet chemical approaches with optimized synthetic parameters have been realized to controllably prepare diverse SAC such as Pt,^{1,4,6,7,9–11,14,16} Au,^{3,8,15,20} Pd,¹³ Rh,^{17,18} Co,¹⁹ etc. For instance, Qiao *et al.* synthesized a 0.17 wt% Pt₁/FeO_x catalyst *via* a coprecipitation method with an optimized precipitating agent at a final pH value.¹ However, the formation mechanism of these SAC remained unknown or controversial, since only a few examples have been investigated thoroughly.

On the other hand, due to the complexity in the structure of metal/metal oxide single atoms, as well as the relatively much lower signals compared to common nanoparticles, advanced characterization techniques are required to precisely detect the electronic and local coordination structures of these single atoms. Among them, aberration-corrected high-angle annular dark-field scanning transmission electron microscopy (HAADF-STEM)^{1–6,8–20} and X-ray absorption fine structure

^aShanghai Synchrotron Radiation Facility, Shanghai Institute of Applied Physics, Chinese Academy of Sciences, Shanghai 201204, China. E-mail: sirui@sinap.ac.cn

^bUniversity of Chinese Academy of Science, Beijing 10049, China

^cKey Laboratory for Colloid and Interface Chemistry, Key Laboratory of Special Aggregated Materials, School of Chemistry and Chemical Engineering, Shandong University, Jinan 250100, China. E-mail: jiacj@sdu.edu.cn

^dCenter for High Resolution Electron Microscopy, College of Materials Science and Engineering, Hunan University, Changsha 410082, China. E-mail: cma@hnu.edu.cn

† Electronic supplementary information (ESI) available: Comparison of the activities, EXAFS result, XANES linear combination fitting result and XPS result. See DOI: 10.1039/c7qi00470b

(XAFS) analysis^{1–3,6–10,12–14,16–20} play crucial roles in determining SAC at the atomic scale, either giving microscopic direct observations or providing macroscopic averaged electronic and local coordination structural information. For example, Guo *et al.* identified three different gold species (single atoms, subnanometer clusters and nanoparticles) on the surface of ceria nanorods by using both HAADF-STEM and XAFS measurements.²⁰

Supported iron (Fe) catalysts have been widely applied, particularly for the Fischer–Tropsch synthesis (FTS) reaction.^{21–26} The previous assignments of the important active species of iron were determined to be either metallic Fe particles^{22,26} or iron carbide (Fe_xC_y) phases such as $\chi\text{-Fe}_5\text{C}_2$ ²⁴ and $\epsilon\text{-Fe}_2\text{C}$.^{23,24} However, to date, the investigations on the effect of ultrafine iron oxide species, which may also be stable and catalytically active for FTS reaction, have been very limited. Meanwhile, nanosized cerium oxide (CeO_2) has been used as a reducible oxide support to deposit different metals or metal oxides because of its easily reversible transformation between Ce^{3+} and Ce^{4+} .^{27,28} Previously, our group prepared finely dispersed iron catalysts on the surface of ceria nanorods *via* a coprecipitation approach, and demonstrated the Fe–O–Fe coordination structure in the form of subnanometer iron oxide clusters as active species for FTS.²⁹

Here we report the creation of single atoms in ceria-supported iron–ruthenium oxide catalysts with the help of the catalytic process of FTS. The harsh reaction conditions (up to 300 °C, 2 MPa, $\text{CO}/\text{H}_2 = 1/1$), normally coarsened small-size clusters into large-size particles, did re-dispersed the subnanometer iron oxide clusters (Fe_xO_y) to generate iron single atoms solely coordinated by oxygen ions. In addition, the introduction of low-concentration (0.5–0.6 at%) Ru effectively accelerated the transformation from the Fe_xO_y clusters to Fe SAC. In this work, the structural evolution of ionic iron single atoms and subnanometer iron oxide clusters has been accurately monitored by not only the HAADF-STEM technique but also the XAFS characterization with the corresponding data analysis.

Results and discussion

In our work, the ceria nanorods were prepared *via* a hydrothermal synthesis. The bimetallic iron–ruthenium oxide sample (**FeRu_Ce**), as well as the corresponding single metal (Fe or Ru) oxide counterpart (**Fe_Ce** or **Ru_Ce**), was anchored onto the surface of ceria nanorods *via* a deposition–precipitation (DP) approach. Table 1 shows that the metal concentrations of Fe are ~10 at%, in good agreement with the designed value. Furthermore, the concentrations of more expensive ruthenium have been determined to be 0.5–0.6 at%, which is much lower than that of cheaper iron. Table 1 also shows that the BET specific surface areas of the as-calcined (air, 400 °C) samples are 92–97 $\text{m}^2 \text{g}^{-1}$, well consistent with those of doped ceria nanorods (80–97 $\text{m}^2 \text{g}^{-1}$).³⁰ It indicates that the doping of metal (Fe and/or Ru) ions did not modify

Table 1 Metal concentrations of Fe and Ru, BET specific surface areas (S_{BET}), lattice constant (a) and averaged particle size (D) of CeO_2 in ceria-supported iron–ruthenium oxide samples

Sample	Fe ^a (at%)	Ru ^a (at%)	S_{BET} ^b ($\text{m}^2 \text{g}^{-1}$)	a^c (Å)	D^d (nm)
FeRu_Ce	9.9	0.6	92	5.399 5.405 ^e	8.9 ± 1.5 8.6 ± 1.4 ^e
Fe_Ce	9.7	—	96	5.401 5.410 ^e	8.4 ± 1.7 8.6 ± 1.6 ^e
Ru_Ce	—	0.5	97	5.407 5.418 ^e	8.5 ± 1.7 8.8 ± 1.7 ^e

^a Determined by ICP-AES. ^b Calculated from the nitrogen adsorption-desorption results. ^c Calculated from XRD patterns. ^d Determined from the HRTEM images with over 100 particles. ^e For used samples.

the textural properties of the CeO_2 support. The X-ray diffraction (XRD) patterns in Fig. 1 verify a pure fcc fluorite-type CeO_2 (JCPDS card no: 34-394) crystal structure for all the ceria-supported iron–ruthenium catalysts after DP, and no phases of $\text{Fe}/\text{Fe}_3\text{O}_4/\text{Fe}_2\text{O}_3$ or Ru/RuO_2 can be identified. The calculated lattice constant (a) of CeO_2 is 5.40–5.41 Å (see Table 1), very close to that of pure ceria nanorods (~5.41 Å) reported in a previous study.³¹

The high-resolution transmission electron microscopy (HRTEM) images in Fig. 2a–c show that all of the fresh samples, either single metal oxide (**Fe_Ce** and **Ru_Ce**) or bimetallic oxide (**FeRu_Ce**), are composed of rod-like nanocrystals with an averaged width (D) of 8.4 to 8.9 nm (see Table 1), in good agreement with that of pure ceria nanorods (8.6 nm).³¹ The HRTEM images also show that these nanorods have been highly crystallized by determining that the d -spacing values match the interplanar distances for CeO_2 (111) planes. Meanwhile, a large number of surface voids can be observed for ceria nanorods in the high-angle annular dark-field scanning transmission electron microscopy (HAADF-STEM) images (Fig. 2d–f), possibly caused by the dehydration process during the hydrothermal growth of CeO_2 .²⁰ Nevertheless, no iron ($\text{Fe}/\text{Fe}_3\text{O}_4/\text{Fe}_2\text{O}_3$) or ruthenium (Ru/RuO_2) crystallized particles were observed in HRTEM, which is consistent with the XRD results.

Aberration-corrected HAADF-STEM combined with electron energy-loss spectroscopy (EELS) measurements was performed to obtain the spatial distribution of Fe in the fresh catalysts. From Fig. 3a, we can see that the Fe-rich microdomains up to

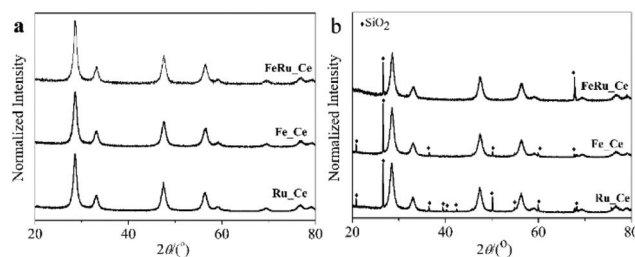


Fig. 1 XRD patterns of fresh (a) and used (b) ceria-supported iron–ruthenium oxide samples.

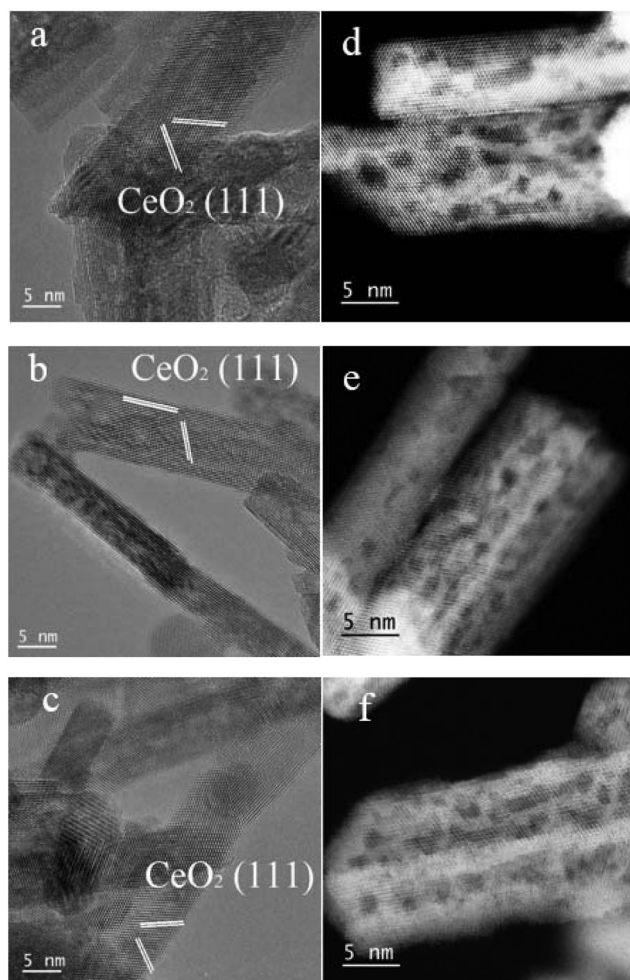


Fig. 2 HRTEM (a–c) and HAADF-STEM (d–f) images of fresh ceria-supported iron–ruthenium oxide samples: (a, d) **Fe_Ce**; (b, e) **Ru_Ce**; and (c, f) **FeRu_Ce**.

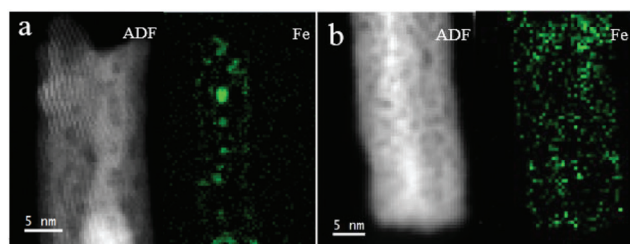


Fig. 3 Aberration-corrected HAADF-STEM/EELS results for fresh ceria-supported iron–ruthenium oxide samples: (a) **Fe_Ce** and (b) **FeRu_Ce**.

ca. 1 nm exist for **Fe_Ce**, which can be attributed to subnanometer iron oxide clusters supported on the surface of ceria.²⁹ For the bimetallic iron–ruthenium oxide sample (**FeRu_Ce**), the distribution of Fe seems to be more uniform (Fig. 3b), possibly due to the smaller size of iron oxide species with the aid of the introduced ruthenium. Due to the distinctly lower *z* value of Fe (*z* = 26) than that of Ce (*z* = 58), as well as the

limited amount of iron (~10 at%) and ruthenium (~0.5 at%) in the measured samples, HAADF-STEM/EELS could only reach a low spatial resolution of *ca.* 2–3 Å in this work. So, the iron single atoms were possibly missing from the microscopic view. Thus, other characterization techniques are required to obtain the specific structure of Fe.

The X-ray absorption fine structure (XAFS) technique is elementally sensitive and very powerful to determine both the electronic structure and local coordination structure (distance (*R*), coordination number (CN), *etc.*) of the investigated metal with the help of X-ray absorption near edge structure (XANES) and extended X-ray absorption fine structure (EXAFS) analyses, respectively. From the XANES profiles in Fig. 4a, with the help of different references (Fe foil for Fe⁰, Fe₃O₄ for Fe²⁺/Fe³⁺ and Fe₂O₃ for Fe³⁺), we have run linear combination fits³² on the fresh catalysts (Fig. S1a and S1b†). Table 2 shows that fully oxidized Fe³⁺ ions, without any fraction of reduced components of Fe²⁺/Fe⁰, can be determined for both single metal (Fe) oxide and bimetallic (Fe, Ru) oxide samples. Besides, the averaged oxidation states of ruthenium in **Ru_Ce** and **FeRu_Ce** are also close to that of ionic Ru³⁺ (Fig. 5a and Fig. S2a, S2b†; Table 3).

On the basis of the EXAFS spectra in the *R* space of the Fe K edge (Fig. 4b), as well as the corresponding fitting results (see Table 2), the local coordination structure around iron can be obtained as follows: (1) a strong peak at 1.96 Å (CN = 4.1–4.5) is assigned to the first shell (Fe–O) for the fresh catalysts; (2) two weak peaks centered at 2.96 and 3.45 Å can be attributed to the second (Fe–Fe) and third shells (Fe–Ce), which originate

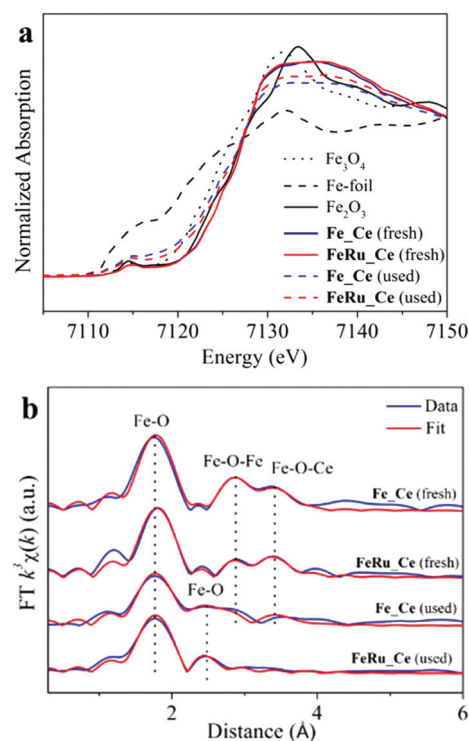
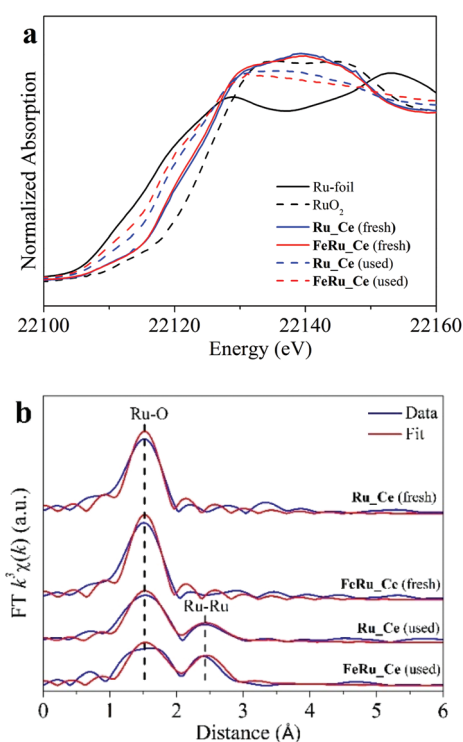


Fig. 4 XANES profiles (a) and EXAFS fitting results in the *R* space (b) for ceria-supported iron–ruthenium oxide samples: Fe K edge.

Table 2 Averaged oxidation state of iron (δ) and Fe K edge EXAFS fitting results (R : distance; CN: coordination number; σ^2 : Debye–Waller factor; ΔE_0 : inner potential correction) of ceria-supported iron–ruthenium oxide samples

Sample	δ^a	Fe–O		Fe–Fe		Fe–Ce		σ^2 (\AA^2)	ΔE_0 (eV)
		R (\AA)	CN	R (\AA)	CN	R (\AA)	CN		
Fe_Ce (fresh)	3.0	1.96 ± 0.01	4.5 ± 0.3	2.96 ± 0.01	2.1 ± 0.5	3.45 ± 0.02	1.6 ± 0.8	0.003(O)	11.2 ± 0.9
Fe_Ce (used)	2.4	1.97 ± 0.01	3.1 ± 0.3	3.07 ± 0.04	0.7 ± 0.4	—	—	0.005(Fe)	9.7 ± 0.9
		2.59 ± 0.02	2.2 ± 0.6						
FeRu_Ce (fresh)	3.0	1.96 ± 0.01	4.1 ± 0.2	2.96 ± 0.01	0.9 ± 0.3	3.45 ± 0.02	1.5 ± 0.5	0.006(Ce)	11.2 ± 0.9
FeRu_Ce (used)	2.7	1.94 ± 0.01	3.4 ± 0.2	—	—	—	—		9.7 ± 0.9
		2.64 ± 0.02	1.1 ± 0.5						
Fe ^b	0	—	—	2.464	8	—	—	—	—
				2.843	6				
Fe ₂ O ₃ ^b	3	1.983	6	2.889	1	—	—	—	—
		2.062	6	2.969	3				
Fe ₃ O ₄ ^b	8/3	2.096	6	2.964	6	—	—	—	—
		3.630	8	3.476	6				

^a Determined by linear combination analysis of the XANES profiles with references of Fe foil ($\delta = 0$) and α -Fe₂O₃ ($\delta = 3$). ^b From Crystallography Open Database (no. 9006603, 1011240 and 1513301 for Fe, Fe₂O₃ and Fe₃O₄, respectively).

**Fig. 5** XANES profiles (a) and EXAFS fitting results in the R space (b) for ceria-supported iron–ruthenium oxide samples: Ru K edge.

from Fe–O–Fe and Fe–O–Ce interactions,²⁹ respectively. These contributions are involved in the Fe_xO_y clusters strongly interacting with the ceria support; (3) the CN of Fe–Fe in FeRu_Ce (0.9) is much lower than that in Fe_Ce (2.1), revealing the presence of a small fraction or a smaller size of Fe_xO_y clusters with the introduction of ruthenium. Furthermore, the EXAFS spectra of our ceria-supported iron–ruthenium oxide catalysts are clearly different from those of the standards (Fe/Fe₂O₃/

Table 3 Averaged oxidation state of ruthenium (δ) and Ru K edge EXAFS fitting results (R : distance; CN: coordination number; σ^2 : Debye–Waller factor^a; ΔE_0 : inner potential correction^b) of ceria-supported iron–ruthenium oxide samples

Sample	δ^c	Ru–O		Ru–Ru	
		R (\AA)	CN	R (\AA)	CN
Ru_Ce (fresh)	3.2	2.00 ± 0.01	4.2 ± 0.4	—	—
Ru_Ce (used)	1.8	2.01 ± 0.02	2.9 ± 0.4	2.71 ± 0.02	1.8 ± 0.4
FeRu_Ce (fresh)	3.1	2.01 ± 0.01	4.4 ± 0.4	—	—
FeRu_Ce (used)	1.3	2.02 ± 0.02	2.4 ± 0.3	2.69 ± 0.02	1.4 ± 0.5
Ru ^d	0	—	—	2.665	6
				2.727	6
RuO ₂ ^d	4	1.942	2		
		1.986	4	3.105	2
		3.412	4	3.539	8
		3.662	4		

^a Set to be 0.003 and 0.006 for Ru–O and Ru–Ru paths, respectively.

^b Determined to be 5.3 ± 1.8 and 4.0 ± 2.7 eV for fresh and used samples, respectively. ^c Determined by linear combination analysis of the XANES profiles with references of Ru foil ($\delta = 0$) and RuO₂ ($\delta = 4$).

^d From Crystallography Open Database (no. 1512537 and 1000058 for Ru and RuO₂, respectively).

Fe₃O₄ and Ru/RuO₂) in the R space (Fig. S3†), which is caused by their small-size cluster nature.

Using the EXAFS spectra in the R space of the Ru K edge (Fig. 5b), as well as the corresponding fitting results (see Table 3), the local coordination structure around ruthenium can be obtained. A strong peak at 2.00–2.01 \AA (CN = 4.2–4.4) is attributed to the Ru–O first shell for both the fresh catalysts, either single metal oxide (Ru_Ce) or bimetallic oxide (FeRu_Ce). No other shells at longer distances can be decided from the EXAFS spectra. This indicates that the ultrafine ruthenium oxide species are highly dispersed over the ceria nanorods.

In this work, the Fischer–Tropsch synthesis (FTS) reaction was tested for different ceria-supported iron–ruthenium oxide

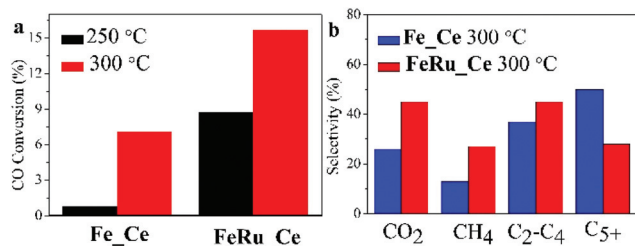
Table 4 Catalytic reactivity of ceria-supported iron–ruthenium samples for FTS

Sample	<i>T</i> (°C)	Conv. ^a (%)	Selectivity ^b (%)				
			CO ₂	CH ₄	C ₂ –C ₄	C ₅ +	Olefin ^c
FeRu_Ce	250	7.1	47	34	52	14	3.1
	300	15.7	45	27	45	28	2.0
Fe_Ce	250	0.8	25	16	41	43	2.6
	300	8.7	26	13	37	50	2.7
Ru_Ce	250	0	—	—	—	—	—
	300	0	—	—	—	—	—

^a Based on carbon calculation under the following reaction conditions: 110 mg, H₂/CO = 1/1, 2.0 MPa, 21.5 ml min^{−1}, time-on-stream of 5 h.

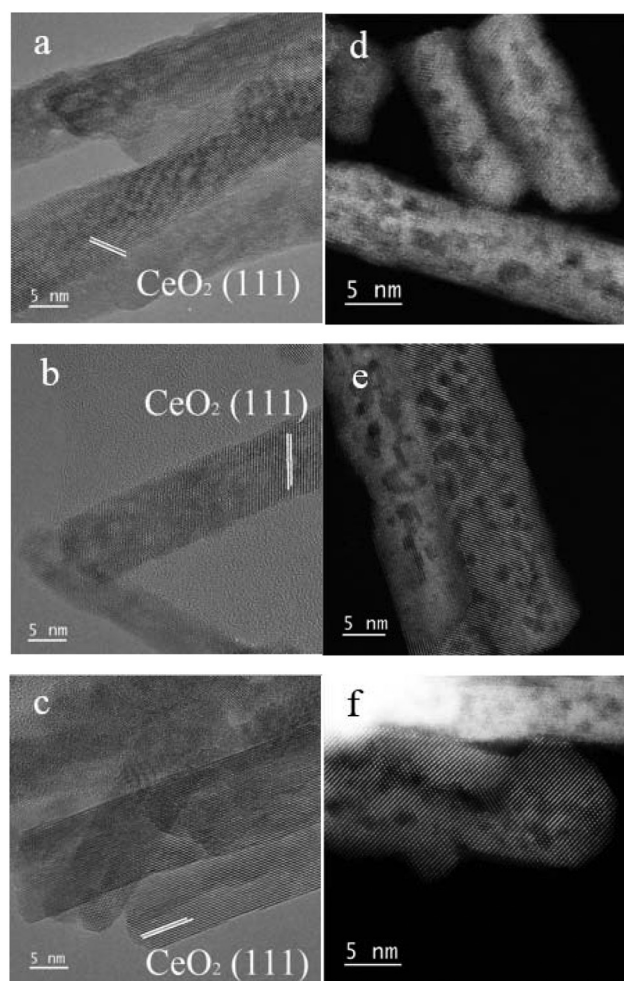
^b Calculation of CO conversion is based on carbon calculation for all hydrocarbons (excluding CO₂). ^c Olefin selectivity is calculated by C₂=C₄/C₂–C₄.

catalysts. Table 4 shows that **Ru_Ce** has zero CO conversion at both temperatures of 250 and 300 °C under the FTS conditions. It has been well known that supported ruthenium catalysts are active for FTS. Carballo *et al.* observed increased TOF values for FTS on 1.8 wt% Ru/Al₂O₃ with an increased Ru particle size from 4 to 16 nm.³³ Recently, Gonzalez-Carballo *et al.* reported a TOF of 0.02 s^{−1} for FTS on Al₂O₃ supported 3 wt% Ru.³⁴ In this work, the very low concentration (*ca.* 0.3 wt%) of Ru in the form of ultrafine clusters (<1–2 nm) prevented the conversion of CO in FTS. Also, the ceria nanorods may not be a good support for the active ruthenium sites in our study, and the catalytic performance of the bimetallic oxide catalyst should be contributed by the active iron sites only. Fig. 6a and Table 4 also show that the CO conversions of **FeRu_Ce** are significantly higher than those of **Fe_Ce** (7.1% *vs.* 0.8% at 250 °C and 15.7% *vs.* 8.7% at 300 °C), nearly one order of magnitude at 250 °C and two orders of magnitude at 300 °C. Table 4 also presents the selectivity of the desired products catalyzed by two different iron-containing samples in FTS at 300 °C. Specifically, the single iron oxide sample (**Fe_Ce**) displays better selectivity than the bimetallic oxide catalyst (**FeRu_Ce**), *e.g.* higher fraction of C₅+, lower percentage of CO₂ and CH₄, as well as nearly identical C₂–C₄. It has been reported that small Ru clusters favor the formation of methane.³⁵ So, the addition of ruthenium did increase the selectivity of methane for our ceria-supported iron oxide catalyst (Table 4). On the other hand, the methane selectivity of iron catalysts supported

**Fig. 6** Catalytic reactivity of ceria-supported iron–ruthenium oxide samples for FTS: (a) CO conversion and (b) selectivity of CO₂, CH₄, C₂–C₄ and C₅ products.

on an inert oxide (*e.g.* Al₂O₃) increases at higher temperature.²¹ However, we used a reducible oxide (CeO₂) support, and thus the methane selectivity decreased slightly (**FeRu_Ce**) or remained constant (**Fe_Ce**) from 250 to 300 °C.²⁹ As discussed above, the distribution of the products on our ceria-supported iron–ruthenium oxide catalysts is modest (see Table S1† for details) and should have no special sites. However, the major motivation of this work is to trace the structural evolution on different species in ceria-supported iron–ruthenium oxide catalysts before and after the FTS reaction.

For the used samples after FTS, we carried out different characterization studies to monitor the structural evolution of ceria-supported iron–ruthenium oxide catalysts. The XRD data (Fig. 1b) showed that the crystal structure of fcc fluorite-type CeO₂ was maintained for the FTS process. There is a minor increase of ceria lattice constants from 5.399–5.407 Å to 5.405–5.418 Å (see Table 1), giving a hint that the surface Fe³⁺ ions may be extracted out of the sub-surface of ceria nanorods under the FTS reaction conditions.²⁹ The HRTEM and HAADF-STEM images (Fig. 7) verified the similar mor-

**Fig. 7** HRTEM (a, b, c) and HAADF-STEM (d, e, f) images of used ceria-supported iron–ruthenium oxide samples: (a, d) **Fe_Ce**; (b, e) **Ru_Ce**; and (c, f) **FeRu_Ce**.

phologies of the used iron–ruthenium oxide catalysts as their fresh counterparts. Meanwhile, the average widths of ceria nanorods show no changes before and after the FTS reaction (see Table 1). Still, no lattice fringes of Fe/Fe₃O₄/Fe₂O₃ or Ru/RuO₂ can be determined.

The aberration-corrected HAADF-STEM/EELS results in Fig. 8 confirm that subnanometer iron oxide species and ruthenium species were dominant in both the iron-containing samples after FTS. The XANES profiles (Fig. 4a and 5a) reveal that both iron and ruthenium species were partially reduced after FTS, with the averaged oxidation states of Fe^{2.4+}, Ru^{1.8+} and Fe^{2.7+}/Ru^{1.3+} for **Fe_Ce**, **Ru_Ce** and **FeRu_Ce**, respectively (see Tables 2 and 3). Here, we found that more oxidized iron species and more reduced ruthenium species were present for the bimetallic oxide sample (**FeRu_Ce**) than those in the single metal oxide counterparts (**Fe_Ce** and **Ru_Ce**). In other words, the relatively lower reduction degree of iron formed at the expense of the relatively higher reduction degree of ruthenium in the used ceria-supported iron–ruthenium oxide catalysts, and thus the introduction of Ru³⁺ could help the stabilization of Fe³⁺ species during FTS. The profiles of XANES linear combination fits for the Fe K edge and Ru K edge have been included (Fig. S1c, S1d, S2c and S2d†).

From Fig. 4b and Table 2, the EXAFS analysis of the Fe K edge for the used catalysts provides the following results: (1) the first shell (Fe–O) is similar to the fresh samples, *i.e.* $R = 1.94\text{--}1.97\text{ \AA}$ and $CN = 3.1\text{--}3.4$; (2) another shell of Fe–O at a longer distance of around 2.6 \AA can be determined for both **Fe_Ce** and **FeRu_Ce** after FTS ($CN = 1.1\text{--}2.2$). The sum of CN values for the above two Fe–O shells is nearly equal to those for the first Fe–O shell before the FTS process, indicating the separation of the Fe–O shell in the used catalysts. This peak-split could be due to the harsh FTS conditions (high pressure and high concentrations of CO/H₂); (3) for the used **Fe_Ce**, the second Fe–Fe shell caused by the Fe–O–Fe interaction is weakened ($CN = 0.7$) and the third Fe–Ce shell around 3.5 \AA caused by the Fe–O–Ce interaction completely disappears, revealing the shrinkage and loss of Fe_xO_y clusters during the FTS reaction for the single metal (Fe) oxide catalyst; (4) for the used **FeRu_Ce**, both Fe–Fe and Fe–Ce shells were lost after FTS. Besides the first Fe–O shell, no contributions in the range of $3\text{--}4\text{ \AA}$ can be identified. Therefore, for ceria-

supported bimetallic iron–ruthenium oxide clusters, Fe single atoms coordinated by oxygen ions only (FeO_x, $R = 1.94$ and 2.64 \AA ; $CN = 3.4$ and 1.1) formed during the FTS process (reaction conditions: up to $300\text{ }^{\circ}\text{C}$, $\text{H}_2/\text{CO} = 1/1$, 2 MPa). Here, the iron oxide clusters observed in the HAADF-STEM/EELS image (Fig. 8b) could be in a minor fraction, and averaged in the EXAFS signals. Furthermore, the missing Fe–Fe metallic bond around 2.5 \AA identifies the absence of the formation of any iron carbide reported by Ribeiro *et al.* previously.³⁶ So, just like the previous studies on the atomically dispersed Pd and cerium oxide,³⁷ the EXAFS analysis probes the short-range ($<4\text{ \AA}$) coordination structure around Fe, as well as identifies the iron SAC in this work. On the other hand, the EXAFS spectra (Fig. 5b) and the related fitting results (Table 3) confirm that both the Ru–O shell ($\sim 2.0\text{ \AA}$, $CN = 2.4\text{--}2.9$) and metallic Ru–Ru bond ($\sim 2.7\text{ \AA}$, $CN = 1.4\text{--}1.8$) are present for the Ru K edge in the used **Ru_Ce** and **FeRu_Ce**, indicating the formation of the metallic Ru–Ru bond in FTS.

It is widely believed that iron carbide (*e.g.* Fe₅C₂) is the active species for FTS.^{23,24,38} In our study, no such Fe₅C₂ species could be determined for the used catalysts, which have been confirmed by the totally different EXAFS spectra from a previous report,³⁸ as well as the almost identical XPS C 1s spectra of **Fe_Ce** and **FeRu_Ce** before and after the reaction (Fig. S4†). The absence of iron carbide is probably due to the lower concentration of Fe (*ca.* 10 at%) in our samples than that for pure Fe₅C₂, and thus the coordinated oxygen species could not be eliminated by carbon during FTS.

As discussed above, the formation of Fe single atoms for ceria-supported bimetallic iron–ruthenium oxide (refer to Scheme 1) was actually governed by the following two key factors: (1) catalytic reaction (FTS) could weaken both the Fe–O–Fe and Fe–O–Ce interactions, *i.e.* the former generates iron oxide clusters, while the latter connects them with the CeO₂ support; here, the real driving forces may be due to the high-concentration of CO or H₂ and the high pressure (*ca.* 2 MPa); and (2) the addition of ruthenium could tune the specific structure of Fe_xO_y clusters, as well as scarify itself (Ru³⁺ → Ru⁰) to prevent the reduction of iron species (Fe³⁺ → Fe⁰).

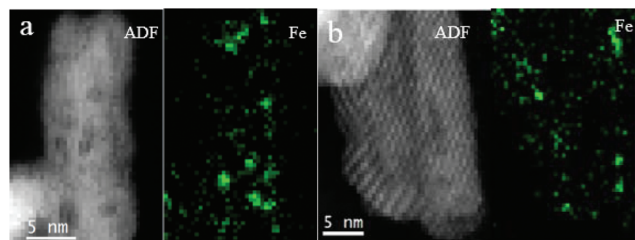
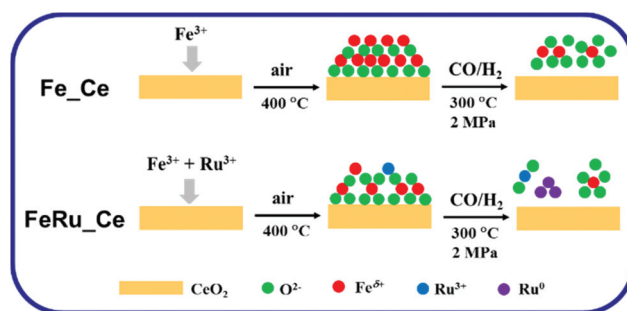


Fig. 8 Aberration-corrected HAADF-STEM/EELS results for used ceria-supported iron–ruthenium oxide samples: (a) **Fe_Ce** and (b) **FeRu_Ce**.



Scheme 1 Demonstration of the formation of Fe single atoms for ceria-supported iron–ruthenium oxide samples.

Conclusions

In conclusion, we have discovered the spontaneous formation of SAC during the FTS process. The electronic and local coordination structures of iron single atoms have been determined by the related XANES analysis and EXAFS fittings, respectively. The high concentration of CO or H₂ and high pressure during FTS could weaken both Fe–O–Fe and Fe–O–Ce interactions for the transformation from iron oxide clusters to iron single atoms. The addition of a small amount of ruthenium could have a positive effect on both catalyst preparation and catalytic reaction steps. All the above factors drove the generation of iron single atoms, which are composed of slightly reduced Fe^{δ+} ($\delta = 2.7$) species coordinated by two different types of oxygen ions at *ca.* 2.0 and 2.6 Å and anchored onto the surface of ceria nanorods.

Experimental

Materials

All the chemicals used in this work were of analytical grade and purchased from Sinopharm Chemical Reagent Co., Ltd without any further purification.

Synthesis

Preparation of ceria nanorods. The ceria nanorods were synthesized according to the hydrothermal method.³⁹ Ce(NO₃)₃·6H₂O (4.5 mmol) was added into an aqueous NaOH (6 M, 60 mL) solution under vigorous stirring. After the precipitation process was completed (about 10 min), the stock solution was transferred into a Teflon bottle, and further tightly sealed in a stainless-steel autoclave. The hydrothermal procedure was carried out in a temperature-controlled electric oven at 100 °C for 24 h. The precipitates were separated by centrifugation and then washed with deionized water four times and ethanol once. The ceria support was obtained by drying the as-washed product in air at 70 °C overnight.

Deposition of iron–ruthenium oxide. Ceria-supported iron–ruthenium oxide samples were synthesized *via* a deposition–precipitation method. (NH₄)₂CO₃ (2.4 g) and the as-calcined CeO₂ nanorods (1 g) were suspended in 100 mL Millipore (>18 MΩ) water under vigorous stirring. Then, Fe(NO₃)₃·9H₂O (0.7 mmol) and RuCl₃·H₂O (0.07 mmol) aqueous solution (15 mL) were added dropwise into the above solution until a final pH value of ~9. After the generation of greenish slurries, the stock solution was further aged at room temperature for another 2 h. The as-obtained precipitates were filtered and then washed with Millipore water three times. The as-washed powders were dried under vacuum at 80 °C overnight and then calcined in air at 400 °C for 4 h (ramping rate: 2 °C min^{−1}).

Characterization

The metal ratios of Fe/Ru/Ce were determined by inductively coupled plasma atomic emission spectroscopy (ICP-AES) on an

IRIS Intrepid II XSP instrument (Thermo Electron Corporation).

Powder X-ray diffraction (XRD) patterns were recorded on a Bruker D8 Advance diffractometer (40 kV, 40 mA) at a scanning rate of 4° min^{−1}, using Cu K_{α1} radiation ($\lambda = 1.5406$ Å). The diffraction patterns were recorded from 20 to 80° with a step of 0.02°. The 2 θ angles were calibrated with a μ m-scale alumina disc. The powder sample after grinding was placed inside a quartz sample holder for each test. The cell dimensions of cubic CeO₂ were calculated from power data with the software “LAPOD” of least-squares refinement by Cohen’s method.^{40,41}

Nitrogen adsorption–desorption measurements were performed on an ASAP2020-HD88 analyzer (Micromeritics Co. Ltd) at 77 K. The measured powders were degassed at 250 °C under vacuum (<100 μ mHg) for over 4 h. The BET specific surface areas (*S*_{BET}) were calculated from the data in the relative pressure range between 0.05 and 0.20.

The aberration-corrected high-resolution TEM (HRTEM) or high-angle annular dark-field scanning transmission electron microscopy (HAADF-STEM) and electron energy-loss spectroscopy (EELS) measurements were performed on a JEOL ARM200F microscope equipped with a probe-forming spherical-aberration corrector and a Gatan image filter (Quantum 965). In order to obtain a good signal-to-noise ratio, the iron distribution was mapped by the Fe L_{2,3} edges in the EELS spectra.

X-ray photoelectron spectroscopy (XPS) analysis was performed on an Axis Ultra XPS spectrometer (Kratos, U.K.) with 225 W of Al K_α radiation (1487 eV). The C 1s line at 284.8 eV was used to calibrate the binding energies.

X-ray absorption fine structure

X-ray absorption fine structure (XAFS) spectroscopy at the Fe K (*E*₀ = 7112 eV) edge and Ru K (*E*₀ = 22 117 eV) edge was performed at the BL14 W1 beamline⁴² of the Shanghai Synchrotron Radiation Facility (SSRF) operated at 3.5 GeV in “top-up” mode with a constant current of 260 mA. The XAFS data were obtained in fluorescence mode with a 7-element Ge solid state detector. The energy was calibrated according to the absorption edge of pure Fe foil and Ru foil.

Athena and Artemis codes were used to extract the data and fit the profiles. For the X-ray absorption near edge structure (XANES) part, the experimental absorption coefficients as a function of energies $\mu(E)$ were processed by background subtraction and normalization procedures, and reported as “normalized absorption”. Based on the normalized XANES profiles, the chemical valence of iron or ruthenium was determined by comparison to the corresponding references of Fe/Fe₂O₃ and Ru/RuO₂.

For the extended X-ray absorption fine structure (EXAFS) part, the Fourier transformed (FT) data in the *R* space of Fe and Ru were analyzed by applying the quick first shell model for the Fe–O, FeO model for Fe–Fe contributions, and by applying the quick first model for the Ru–O, Ru model for Ru–Ru contributions. The passive electron factor, *S*₀², was determined by fitting the experimental data on Fe and Ru foils and fixing

the coordination number (CN) of Fe–Fe to be 8 + 6 and that of Ru–Ru to be 12, and then fixing for further analysis of the measured samples. The parameters describing the electronic properties (e.g., correction to the photoelectron energy origin, E_0) and the local structure environment including the CN, bond distance (R) and Debye–Waller (DW) factor around the absorbing atoms were allowed to vary during the fitting process. The fitted ranges for the k and R spaces were selected to be $k = 2.7\text{--}9.7 \text{ \AA}^{-1}$ with $R = 0.8\text{--}3.6 \text{ \AA}$ (k^3 weighted) for the Fe K edge and $k = 3\text{--}10 \text{ \AA}^{-1}$ with $R = 0.8\text{--}3.3 \text{ \AA}$ (k^2 weighted) for the Ru K edge. To distinguish the effect of the Debye–Waller factor from that of the coordination number, we set σ^2 to be 0.003, 0.005 and 0.006 \AA^2 for all the analyzed Fe–O, Fe–Fe and Fe–Ce shells, respectively, according to the fitted results of iron standards. We also set σ^2 to be 0.003 and 0.006 \AA^2 for all the analyzed Ru–O and Ru–Ru shells, according to the fitted results of ruthenium standards. To distinguish the effect of the correction to the photoelectron energy origin from that of the distance, we set ΔE_0 to be 11.2/9.7 eV for fresh/used **Fe_Ce** and **FeRu_Ce** (Fe K edge) and 5.3/4.0 eV for fresh/used **Ru_Ce** and **FeRu_Ce** (Ru K edge), which were obtained from the linear combination fits on the XANES profiles and the fitting results of the standards.

Catalytic tests

The catalytic activity of the Fischer–Tropsch synthesis (FTS) reaction of the ceria-supported iron–ruthenium oxide samples was investigated in a fixed-bed flow reactor using 110 mg of sieved (40–60 mesh) powders diluted with 0.5 g SiO₂ in a gas mixture of 47 vol% CO, 47 vol% H₂ and 6 vol% N₂ (from Jinan Deyang Corporation, 99.997% purity) at a flow rate of 21.7 mL min^{−1}, corresponding to a space velocity of 12 000 mL h^{−1} g_{cat}^{−1}. The FTS measurements at multiple temperatures (250–300 °C) were carried out at a high pressure of 2 MPa with a pretreatment at 350 °C for 3 h in 10% H₂/Ar.

The product and reactant in the gas phase were detected online using a gas chromatograph (GC-9160, Shanghai, China). C₁–C₄ range hydrocarbons were analyzed using a Plot Al₂O₃ capillary column with a flame ionization detector (FID); however, CO, CO₂, CH₄, and N₂ were analyzed by using a Porapak Q and 5A molecular sieve-packed column with a thermal conductivity detector (TCD). To calculate the CO conversion, the 6% N₂ in syngas was used as an internal standard. All hydrocarbons were analyzed using a GC-9160 with a PONA capillary column and a flame ionization detector (FID). The selectivity of the products was calculated on the basis of all used CO, whereas the selectivity of CH₄, C₂–C₄, and C₅⁺ was calculated on the basis of all hydrocarbons produced.

Conflicts of interest

There are no conflicts to declare.

Acknowledgements

This work was financially supported by the National Science Foundation of China (NSFC) (grant no. 21373259), the Excellent Young Scientists Fund from the NSFC (21622106), the Hundred Talents Project of the Chinese Academy of Sciences, the Strategic Priority Research Program of the Chinese Academy of Sciences (grant no. XDA09030102), the Taishan Scholar Project of Shandong Province (China), and the Fundamental Research Funds for the Central Universities (China).

Notes and references

- 1 B. T. Qiao, A. Q. Wang, X. F. Yang, L. F. Allard, Z. Jiang, Y. T. Cui, J. Y. Liu, J. Li and T. Zhang, *Nat. Chem.*, 2011, **3**, 634–641.
- 2 X. G. Guo, G. Z. Fang, G. Li, H. Ma, H. J. Fan, L. Yu, C. Ma, X. Wu, D. H. Deng, M. M. Wei, D. L. Tan, R. Si, S. Zhang, J. Q. Li, L. T. Sun, Z. C. Tang, X. L. Pan and X. H. Bao, *Science*, 2014, **344**, 616–619.
- 3 M. Yang, S. Li, Y. Wang, J. A. Herron, Y. Xu, L. F. Allard, S. Lee, J. Huang, M. Mavrikakis and M. Flytzani-Stephanopoulos, *Science*, 2014, **346**, 1498–1501.
- 4 M. Yang, J. L. Liu, S. Lee, B. Zugic, J. Huang, L. F. Allard and M. Flytzani-Stephanopoulos, *J. Am. Chem. Soc.*, 2015, **137**, 3470–3473.
- 5 J. Jones, H. F. Xiong, A. T. Delariva, E. J. Peterson, H. Pham, S. R. Challa, G. S. Qi, S. Oh, M. H. Wiebenga, X. I. P. Hernandez, Y. Wang and A. K. Datye, *Science*, 2016, **353**, 150–154.
- 6 L. L. Lin, W. Zhou, R. Gao, S. Y. Yao, X. Zhang, W. Q. Xu, S. J. Zheng, Z. Jiang, Q. L. Yu, Y. W. Li, C. Shi, X. D. Wen and D. Ma, *Nature*, 2017, **544**, 80–83.
- 7 H. Itoi, H. Nishihara, S. Kobayashi, S. Ittisanronnachai, T. Ishii, R. Berenguer, M. Ito, D. Matsumura and T. Kyotani, *J. Phys. Chem. C*, 2017, **121**, 7892–7902.
- 8 S. Yao, X. Zhang, W. Zhou, R. Gao, W. Xu, Y. Ye, L. Lin, X. Wen, P. Liu, B. Chen, E. Crumlin, J. Guo, Z. Zuo, W. Li, J. Xie, L. Lu, C. J. Kiely, L. Gu, C. Shi, J. A. Rodriguez and D. Ma, *Science*, 2017, **357**, 389–393.
- 9 B. Zhang, H. Asakura, J. Zhang, J. G. Zhang, S. De and N. Yan, *Angew. Chem., Int. Ed.*, 2016, **55**, 8319–8323.
- 10 S. G. Yang, J. Kim, Y. J. Tak, A. Soon and H. Lee, *Angew. Chem., Int. Ed.*, 2016, **55**, 2058–2062.
- 11 Z. P. Chen, S. Mitchell, E. Vorobyeva, R. K. Leary, R. Hauert, T. Furnival, Q. M. Ramasse, J. M. Thomas, P. A. Midgley, D. Dontsova, M. Antonietti, S. Pogodin, N. Lopez and J. Perez-Ramirez, *Adv. Funct. Mater.*, 2017, **27**, 1605785.
- 12 H. Yan, H. Cheng, H. Yi, Y. Lin, T. Yao, C. L. Wang, J. J. Li, S. Q. Wei and J. L. Lu, *J. Am. Chem. Soc.*, 2015, **137**, 10484–10487.
- 13 P. X. Liu, Y. Zhao, R. X. Qin, S. G. Mo, G. X. Chen, L. Gu, D. M. Chevier, P. Zhang, Q. Guo, D. D. Zang, B. H. Wu, G. Fu and N. F. Zheng, *Science*, 2016, **352**, 797–801.

- 14 S. G. Yang, Y. J. Tak, J. Kim, A. Soon and H. Lee, *ACS Catal.*, 2017, **7**, 1301–1307.
- 15 B. Qiao, J. X. Liu, Y. G. Wang, Q. Q. Lin, X. Y. Liu, A. Q. Wang, J. Li, T. Zhang and J. Liu, *ACS Catal.*, 2015, **5**, 6249–6254.
- 16 H. Huang, K. Li, Z. Chen, L. Luo, Y. Gu, D. Zhang, C. Ma, R. Si, J. Yang, Z. Peng and J. Zeng, *J. Am. Chem. Soc.*, 2017, **139**, 8152–8159.
- 17 L. B. Wang, W. B. Zhang, S. P. Wang, Z. H. Gao, Z. H. Luo, X. Wang, R. Zeng, A. W. Li, H. L. Li, M. L. Wang, X. S. Zheng, J. F. Zhu, W. H. Zhang, C. Ma, R. Si and J. Zeng, *Nat. Commun.*, 2016, **7**, 14036.
- 18 L. B. Wang, H. L. Li, W. B. Zhang, X. Zhao, J. X. Qiu, A. W. Li, X. S. Zheng, Z. P. Hu, R. Si and J. Zeng, *Angew. Chem., Int. Ed.*, 2017, **56**, 4712–4718.
- 19 P. Q. Yin, T. Yao, Y. Wu, L. R. Zheng, Y. Lin, W. Liu, H. X. Ju, J. F. Zhu, X. Hong, Z. X. Deng, G. Zhou, S. Q. Wei and Y. D. Li, *Angew. Chem., Int. Ed.*, 2016, **55**, 10800–10805.
- 20 L. W. Guo, P. P. Du, X. P. Fu, C. Ma, J. Zeng, R. Si, Y. Y. Huang, C. J. Jia, Y. W. Zhang and C. H. Yan, *Nat. Commun.*, 2016, **7**, 13481.
- 21 H. H. Dong, M. J. Xie, J. Xu, M. F. Li, L. M. Peng, X. F. Guo and W. P. Ding, *Chem. Commun.*, 2011, **47**, 4019–4021.
- 22 H. M. T. Galvis, J. H. Bitter, T. Davidian, M. Ruitenbeek, A. I. Dugulan and K. P. de Jong, *J. Am. Chem. Soc.*, 2012, **134**, 16207–16215.
- 23 R. P. Mogorosi, N. Fischer, M. Claeys and E. van Steen, *J. Catal.*, 2012, **289**, 140–150.
- 24 K. Xu, B. Sun, J. Lin, W. Wen, Y. Pei, S.-R. Yan, M.-H. Qiao, X.-X. Zhang and B.-N. Zong, *Nat. Commun.*, 2014, **5**, 5783.
- 25 J. Z. Lu, L. J. Yang, B. L. Xu, Q. Wu, D. Zhang, S. J. Yuan, Y. Zhai, X. Z. Wang, Y. N. Fan and Z. Hu, *ACS Catal.*, 2014, **4**, 613–621.
- 26 V. Iablokov, Y. Xiang, A. Meffre, P.-F. Fazzini, B. Chaudret and N. Kruse, *ACS Catal.*, 2016, **6**, 2496–2500.
- 27 Q. Fu, H. Saltsburg and M. Flytzani-Stephanopoulos, *Science*, 2003, **301**, 935–938.
- 28 S. Carrettin, P. Concepcion, A. Corma, J. M. L. Nieto and V. F. Puentes, *Angew. Chem., Int. Ed.*, 2004, **43**, 2538–2540.
- 29 Q. Yang, X.-P. Fu, C.-J. Jia, C. Ma, X. Wang, J. Zeng, R. Si, Y.-W. Zhang and C.-H. Yan, *ACS Catal.*, 2016, **6**, 3072–3082.
- 30 W. W. Wang, P. P. Du, S. H. Zou, H. Y. He, R. X. Wang, Z. Jin, S. Shi, Y. Y. Huang, R. Si, Q. S. Song, C. J. Jia and C. H. Yan, *ACS Catal.*, 2015, **5**, 2088–2099.
- 31 R. Si, J. Raitano, N. Yi, L. Zhang, S.-W. Chan and M. Flytzani-Stephanopoulos, *Catal. Today*, 2012, **180**, 68–80.
- 32 A. I. Frenkel, Q. Wang, N. Marinkovic, J. G. Chen, L. Barrio, R. Si, A. L. Camara, A. M. Estrella, J. A. Rodriguez and J. C. Hanson, *J. Phys. Chem. C*, 2011, **115**, 17884–17890.
- 33 J. M. G. Carballo, J. Yang, A. Holmen, S. Garcia-Rodriguez, S. Rojas, M. Ojeda and J. L. G. Fierro, *J. Catal.*, 2011, **284**, 102–108.
- 34 J. M. Gonzalez, F. J. Perez-Alonso, F. J. Garcia-Garcia, M. Ojeda, J. L. G. Fierro and S. Rojas, *J. Catal.*, 2015, **332**, 177–186.
- 35 M. C. Bahome, L. L. Jewell, K. Padayachy, D. Hildebrandt, D. Glasser, A. K. Datye and N. J. Coville, *Appl. Catal., A*, 2007, **328**, 243–251.
- 36 M. C. Ribeiro, G. Jacobs, B. H. Davis, D. C. Cronauer, A. J. Kropf and C. L. Marshall, *J. Phys. Chem. C*, 2010, **114**, 7895–7903.
- 37 P.-P. Du, X.-C. Hu, X. Wang, C. Ma, M. Du, J. Zeng, C.-J. Jia, Y.-Y. Huang and R. Si, *Inorg. Chem. Front.*, 2017, **4**, 668–674.
- 38 C. Yang, H. B. Zhao, Y. L. Hou and D. Ma, *J. Am. Chem. Soc.*, 2012, **134**, 15814–15821.
- 39 H.-X. Mai, L.-D. Sun, Y.-W. Zhang, R. Si, W. Feng, H.-P. Zhang, H.-C. Liu and C.-H. Yan, *J. Phys. Chem. B*, 2005, **109**, 24380–24385.
- 40 J. I. Langford, *J. Appl. Crystallogr.*, 1971, **4**, 259–260.
- 41 J. I. Langford, *J. Appl. Crystallogr.*, 1973, **6**, 190–196.
- 42 H. S. Yu, X. J. Wei, J. Li, S. Q. Gu, S. Zhang, L. H. Wang, J. Y. Ma, L. N. Li, Q. Gao, R. Si, F. F. Sun, Y. Wang, F. Song, H. J. Xu, X. H. Yu, Y. Zou, J. Q. Wang, Z. Jiang and Y. Y. Huang, *Nucl. Sci. Tech.*, 2015, **26**, 050102.